

Secondary flows and developing, turbulent boundary layers in a rotating duct

By I. MACFARLANE, P. N. JOUBERT AND T. B. NICKELS

Department of Mechanical and Manufacturing Engineering, The University of Melbourne,
Parkville, Victoria 3052, Australia

(Received 11 April 1997 and in revised form 6 May 1998)

The work presented in this paper represents an experimental investigation into secondary flows, turbulent boundary layers and the interaction of the two as they develop in a zero-pressure-gradient rotating flow field. A duct of intermediate aspect ratio was used to examine secondary flows and determine when they begin to govern the boundary layer development. The aspect ratio (A) was defined as duct height/width at the upstream end of the working section. Measurements were taken at three aspect ratios: $A = 1, 2$ and 4 .

A qualitative indication of secondary flow strength was established with mean-cross-stream-plane velocity measurements. A first-order analysis of the secondary flow is presented which provides a reasonable estimation of their strength. Mid-span mean-flow, turbulence and spectra profiles were measured on the duct walls parallel to the axis of rotation. Results are generally presented for $A = 2$ and 1 . For $A = 4$ and 2 there were minor effects of secondary flows observed on the mid-span mean flow parameters. The turbulent shear measurements showed some secondary flow effect for $A = 2$. All turbulence and mean-flow quantities were strongly affected by secondary flows for $A = 1$. Spectra results presented for $A = 2$ showed most variation at the low-to-mid wavenumber end. Spectra results for $A = 1$ showed a bodily shift of the whole spectrum towards low wavenumber on the pressure side and high wavenumber on the suction side.

1. Introduction

1.1. Literature review

This section will outline previous work in the area of rotating boundary layers. The small amount of experimental data available for this flow case will be highlighted, together with the aims of the current investigation.

There have been several experimental investigations in high-aspect-ratio experimental apparatus. In these cases, the secondary flows are sufficiently removed from the mid-span boundary layers to allow study of the Coriolis instability in isolation from the Ekman layers. There have also been several studies in low-aspect-ratio ducts, where the secondary flow effects dominate the boundary layer development. The current study investigates the intermediate aspect ratios and evaluates when the secondary flow effects begin to govern the flow.

In a high-aspect-ratio rotating duct with zero pressure gradient, Watmuff, Witt & Joubert (1985) and Witt (1986) found that the boundary layer developed with suppressed mean-flow quantities on the suction side compared with the zero rotation case and enhanced mean-flow quantities on the pressure side. The turbulence quantities

showed effects similar to that of increased development length for the pressure side and decreased development length for the suction side. The aspect ratio of the duct used in these experiments was 4:1 (height:width). The turbulence results presented were Reynolds normal and shear stresses.

With the same inlet aspect ratio (4:1), Ibal & Joubert (1995) and Ibal (1990) studied boundary layers subjected to adverse pressure gradients (APG) and rotation. Ibal studied a 'weak' APG case (sidewalls diverging at 3°) and a 'strong' APG case (sidewalls diverging at 8°). Thorough boundary layer measurements were presented, including Reynolds normal and shear stresses, triple products, shear stress and energy balances. In general, the conclusions of his study agreed with those of Watmuff *et al.* (1985), namely stabilized flow on the suction side and destabilized flow on the pressure side. For the strong APG case opposite trends were observed at station 2. It was concluded that flow separation on the opposite sidewall was the more likely cause. However, no attempt was made to clarify the effects of secondary flows on the boundary layer development. This effect was most probably significant at least at the downstream stations of the diffuser. As such it is not possible to determine from the results which effects were attributable to the APG, Coriolis force or secondary flows.

Kikuyama *et al.* (1986) studied the effects of rotation in a plane diffuser but with radial inward flow, opposite to other studies. The diffuser angles studied were 0° , 2.5° and 5° . Obviously the zero angle diffuser is close to the case of the current study, although a slight favourable pressure gradient was observed due to the growth of the boundary layer displacement thickness. The inlet aspect ratio was 4:1, presumably height:width although this was not explicit. If the aspect ratio was 1:4 then the height of their duct was 7 mm. Measurements in the straight-walled duct showed boundary layer growth promoted on the suction side and suppressed on the pressure side at all stations, opposite to the results of other workers in the same aspect ratio; this result remains unexplained. An aspect ratio of 1:4 would make their results more consistent. Also, the turbulence results presented at the inlet showed some unusual behaviour. The stationary turbulence levels were almost twice that of Klebanoff (1955) and this must be considered when interpreting the results. Their conclusions with respect to turbulence levels seem at odds with what is shown in their graphs. Again, no attempt was made to clarify the secondary flow effects and turbulence quantities were limited to Reynolds normal and shear stress components.

The effects of system rotation on developing turbulent boundary layers on the sidewalls of low-aspect-ratio rotating rectangular channels were studied by Hill & Moon (1962) and Moon (1964). The aspect ratio of the ducts in these experiments was 2:3 and 2:1 respectively. The mean-flow measurements showed that boundary layer growth was promoted on the suction side and suppressed on the pressure side. Measurements of streamwise and wall normal turbulence intensities showed an increase on the pressure side and a decrease on the suction side. Turbulent shear stress was substantially increased on the pressure side of the duct. This is in agreement with the conclusions of the preliminary report presented by Koyoma, Tamura & Saito (1989) who were conducting experiments in a 1:7 (height:width) low-aspect-ratio rotating channel. The boundary layer growths were contrary to the findings of Watmuff *et al.* (1985).

The differing trends observed in boundary layer mean-flow properties mentioned above can be explained as follows. In higher-aspect-ratio experimental rigs, secondary flow effects are sufficiently removed from the centreline velocity profiles to provide negligible influence. In the lower aspect ratios, secondary flows are sufficiently close to the centreline profiles to overcome the Coriolis instability. The above studies have been

performed in isolation and to date there have been no studies conducted which provide direct comparison of results with differing secondary flow effects on developing turbulent boundary layers.

The relative importance of the Coriolis instability and the large-scale secondary circulations on fully developed turbulent duct flow was investigated by Moore (1967). He found mid-span velocity and turbulence profiles to be significantly affected by the secondary flows in aspect-ratios of $\frac{1}{2}:1$ and $1:1$, while $4:1$ and $7\frac{1}{2}:1$ were little affected.

1.2. Background theory

The Reynolds stress development equations show how streamline convergence and rotation influence the development of the Reynolds stress components. The equations are

$$\frac{D(-\overline{uw})}{Dt} = \overline{v^2} \frac{\partial U}{\partial y} + (-\overline{uw}) \frac{\partial W}{\partial z} + (\overline{u^2} - \overline{v^2}) 2\Omega + OT, \quad (1.1)$$

$$\frac{D(\overline{u^2})}{Dt} = (-\overline{uw}) \frac{\partial U}{\partial y} - 2\Omega(-\overline{uw}) + OT, \quad (1.2)$$

$$\frac{D(\overline{v^2})}{Dt} = \overline{v^2} \frac{\partial V}{\partial y} + 2\Omega(-\overline{uw}) + OT, \quad (1.3)$$

$$\frac{D(\overline{w^2})}{Dt} = -\overline{vw} \frac{\partial W}{\partial y} - \overline{w^2} \frac{\partial W}{\partial z} + OT, \quad (1.4)$$

where D/Dt represents the total derivative and OT are other terms found in the stationary flow case. For details of the derivation and OT refer to Townsend (1976). In the current flow case D/Dt reduces to $U\partial/\partial x + V\partial/\partial y$ since we have steady flow with $W = 0$ and $\partial W/\partial z \neq 0$ on the centre line.

From the above equations it can be seen that the shear stress is directly affected by both rotation and the extra strain rate $\partial W/\partial z$. The $\overline{u^2}$ and $\overline{v^2}$ stresses are directly affected by rotation terms, but not directly affected by the extra strain rate $\partial W/\partial z$. These stresses are indirectly affected by the extra strain rate through its influence on the shear stress. The $\overline{w^2}$ stress is not directly affected by rotation but is directly affected by $\partial W/\partial z$. The turbulence results will be discussed in terms of equations (1.1)–(1.4). An expanded discussion can be found in Macfarlane (1997).

2. Apparatus and techniques

The open return tunnel used in the experiments has been described in numerous previous publications. An elevation of the apparatus can be found in Watmuff *et al.* (1985) or Macfarlane & Joubert (1996). Air flow was provided by a two stage axial fan located on the floor above the rotating assembly. The air passed through rotating ductwork fitted with turning vanes, honeycombs and screens to ensure that the flow was approximately irrotational relative to the duct at the working section entry. Care has been taken to ensure that the working section boundary layers in the zero rotation case are two-dimensional. Power, control and data signals were all provided to the rotating rig through high-quality slip rings. Data signals were all amplified prior to transmission through the slip rings to maximize signal-to-noise ratio.

Figure 1 shows an isometric sketch of the working section. It defines the coordinate system used and the pressure and suction sidewalls for the direction of rotation shown.

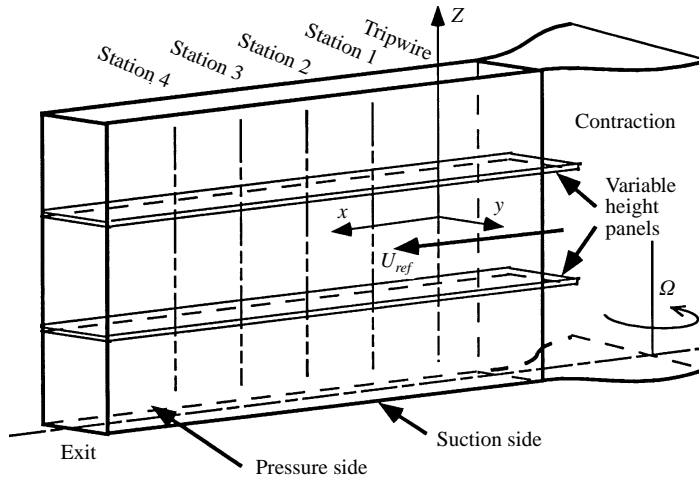


FIGURE 1. Isometric view of working section.

In order to study pressure and suction-side behaviour, the direction of tunnel rotation was reversed. Positive rotation corresponded to the pressure side and negative to the suction side. U is the mean component of velocity in the x or streamwise direction. Fluctuating velocity components are u , v and w in the x -, y - and z -directions respectively. Overbars (e.g. $\overline{u^2}$) represent time-averaged quantities.

The full working section of 600 mm high and 150 mm wide was used for height:width aspect ratio $A = 4$. Two horizontal plates were fitted into the working section, symmetrically about the centreline to provide the reduced aspect ratios. The plates extended upstream approximately 75 mm into the contraction.

The free-stream turbulence intensity at the working section entrance was less than 0.15% for stationary cases and 0.35% with rotation. A stepping motor traverse mechanism mounted on one side of the working section traversed probes through the boundary layer on the opposite wall. The pressure gradient C_p for all aspect ratios was adjusted to within $\pm 0.5\%$ for the stationary case. C_p was not significantly affected by rotation. To allow for daily variation in temperature and pressure, the tunnel velocity was set to a unit Reynolds number/metre of $Re_{ref} = U_R/\nu = 664000 \pm 0.5\%$. This corresponded to a nominal reference velocity U_R of 10 m s^{-1} . The rotation rate of the tunnel was set to 60 r.p.m., giving a Rossby number range of $Ro_x = U_R/\omega X = 1.6$ to 5.3. The boundary layers were tripped by a 1.2 mm diameter trip wire.

2.1. Skin friction measurements

Wall shear velocity and skin friction measurements were made with a 1.0 mm diameter Preston tube. The value of y^+ for the Preston tube ranged from approximately 30 to 50 for the various cases. The calculation method used for evaluating skin friction was that outlined in Patel (1965).

2.2. Mean-flow measurements

Mean-flow results presented here were measured with a 0.6 mm diameter total head tube and a wall static pressure tapping. The method outlined by Johnson, Halleen & Lezius (1972) was used to correct rotating results for the nonlinear static pressure variation across the duct. The wall normal distance was corrected to allow for proximity of the total head probe to the wall. The correction used was that of

MacMillan (1956). Mean-flow results were repeated with a normal hot-wire anemometer. Results obtained with the two methods generally agreed to better than 2%.

2.3. Hot-wire anemometry

Constant-temperature hot-wire anemometers were used for normal and cross-wire measurements. A brief description is given here as full details of the equipment and calibration techniques can be found in Perry (1982). Details specific to the rotating wind tunnel can be found in Macfarlane (1997).

A 1 mm long 5 μ m diameter sensing element of pure platinum was used at an overheat ratio of 2.0. The frequency response of the system was found from square-wave injection tests. During the test the anemometers were adjusted for optimum damping at the lowest velocity. The frequency response was then determined and was in all cases better than 20 kHz. All hot-wire electronics were placed on the rotating apparatus and signals were amplified prior to transmission through the slip rings.

A dynamic calibration procedure was used for calibrating the wires. This involved shaking the wire at a known small velocity perturbation in the U -direction (and V -direction for cross-wires) at discrete points over the range of mean velocities anticipated in the experiment. For small perturbations, the sensitivities $\partial U/\partial E_u$ may be taken as u/e_u , where E_u is the output voltage of the anemometer and u and e_u are the r.m.s. quantities of the perturbations in U and E_u . A third-order polynomial calibration equation was inferred from the sensitivities. This method of calibration accounts for the nonlinearity of the hot-wire system and does not rely on any heat transfer laws. The initial wall distance of the wires was established using an electrical contact between the probe and a pin on the wall. The distance was measured with a graticule microscope at the point when the contact was broken as the probe moved away from the wall. The distance was assumed to be the same with the tunnel rotating. The wall contact was also useful in establishing that deflection or vibration of the probe with rotation was negligible.

2.4. Spectra

Spectra were measured with matched but uncalibrated normal and cross-wire probes. Velocity signals were sampled and their Fourier transforms found using a fast Fourier transform (FFT) algorithm. In order to obtain an acceptable frequency bandwidth, three sampling rates were used (namely 500 Hz, 5 kHz and 40 kHz). To avoid aliasing problems the velocity signals were filtered at 0.4 times the sampling rate. The three files were then smoothed, joined and the final result interpolated to provide equi-spaced points in logarithmic coordinates. Further details of the method used to measure spectra can be found in Macfarlane (1997).

3. Results

3.1. Cross-stream-plane mean-velocity measurements

A series of measurements were taken at station 1 and station 4, for the three aspect-ratio cases studied. These measurements were made with a cross-wire probe oriented in ' uv ' mode and then ' uw ' mode. The two files obtained were then merged and a mean cross-stream plane vector field produced. The results were used to qualitatively estimate the secondary flow effects on the mid-span boundary layers. They were also used in a first-order analysis of the secondary flow effects in an attempt to quantify secondary flow strength in a rotating flow.

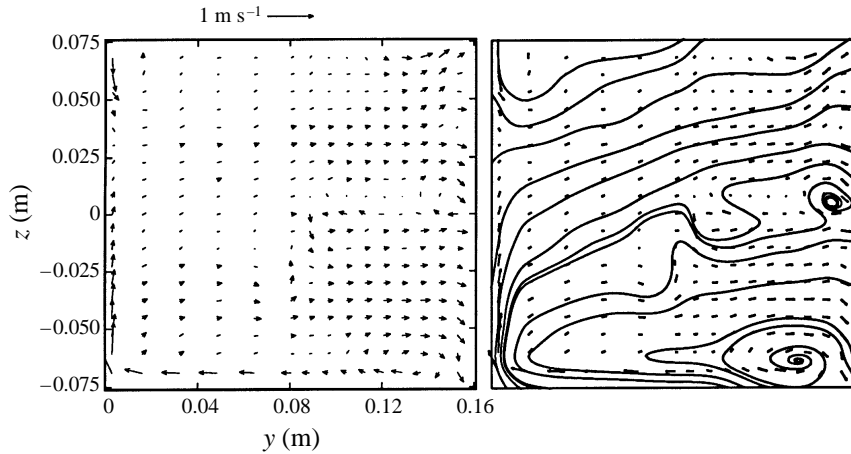


FIGURE 2. Mean cross-stream-plane vector field and streamlines. Station 1, $A = 1$. Flow out of page. Suction side at $y = 0$ as shown in figure 8.

3.1.1. Presentation of cross-stream-plane data

The data at each station are presented as a plain vector plot and also with an integrated streamline pattern. The box around each plot represents the tunnel walls at that measurement station. Careful inspection of the plots reveal that the aspect ratios shown do not exactly reflect the titles ‘ $A = 4$ ’, ‘ $A = 2$ ’ and ‘ $A = 1$ ’. As previously mentioned the sidewalls of the duct were slightly diverging to maintain zero pressure gradient. The divergence accounts for the increasing boundary layer displacement thickness with streamwise development. The divergence of the sidewalls results in the aspect ratio (height to width) reducing slightly with streamwise distance.

The resolution of the measurement grid was selected to ensure that the secondary flow effects could be seen in the results, while ensuring that the experiments would be completed in a reasonable period of time (considering anemometer drift, ambient temperature and pressure variations, etc.). The longer experiments at $A = 2$ and $A = 4$ ran for approximately 8 to 9 hours. The grid used was not sufficiently fine to resolve the pressure-side roll cell pattern.

3.1.2. Accuracy of cross-stream-plane measurements

The accuracy of the measurements is reliant on minimizing drift in the hot-wire calibration and ensuring correct orientation of the probe relative to the free stream between the calibrating and measurement wind tunnels. Mechanical devices were used to ensure that alignment was repeatable in each of the tunnels. Each time the probe was calibrated and then transferred to the measurement wind tunnel, alignment was finally set by ensuring the hot-wire system output voltage, E_v , was within 5 mV, at the same nominal value of E_u . The anemometer calibration was checked at the beginning and end of each experiment as discussed in §2. In the cross-stream-plane measurements the run was rejected if drift in the calibration was more than 2% in mean flow.

Physical constraints of the probe restricted measurements near the top and pressure sidewalls. For station 1 measurements, the probe was unable to be moved sufficiently close to the wall to measure within the boundary layer and hence was unable to measure the secondary flow toward the suction sidewall. Therefore the vortex associated with the top wall secondary flow is not evident in the vector plots or streamline patterns at station 1. Physical constraints of the traverse mechanism restricted measurements to the lower half of the duct for $A = 4$.

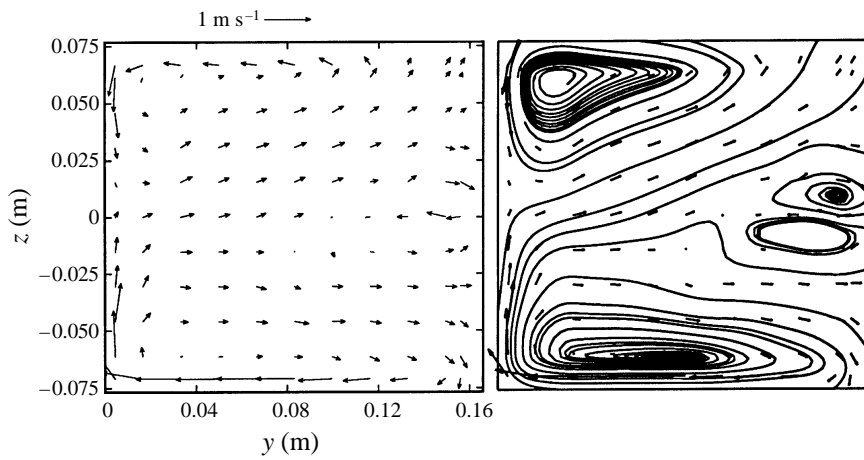
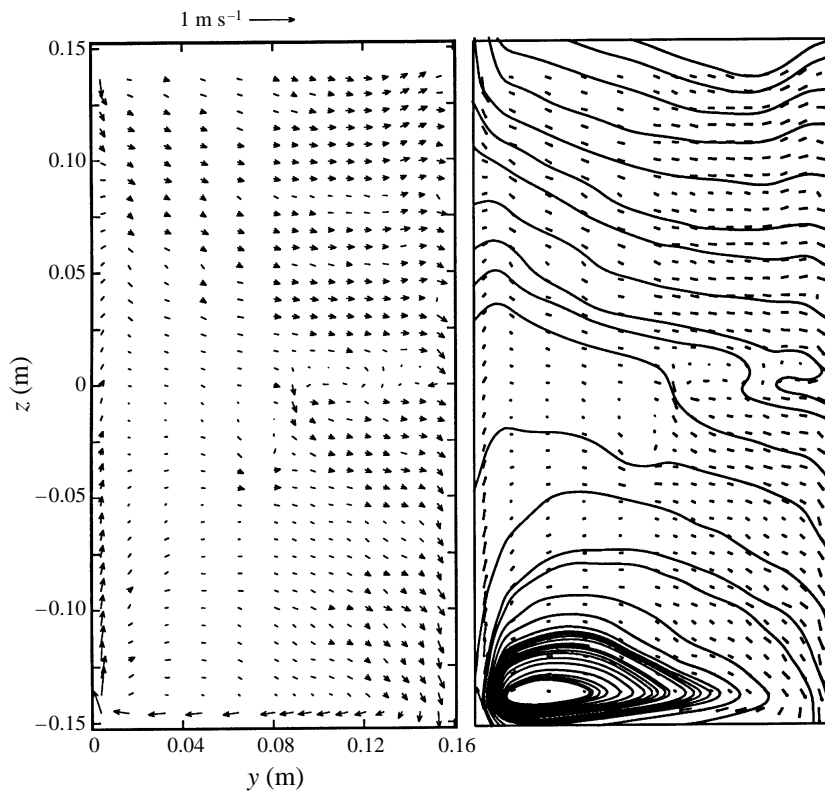


FIGURE 3. As figure 2 but at Station 4.

FIGURE 4. Mean cross-stream-plane vector field and streamlines. Station 1, $A = 2$. Flow out of page. Suction side at $y = 0$ as shown in figure 8.

The cross-stream flow results reveal a slight asymmetry in the flow pattern for $A = 2$ and $A = 1$. It appears that the bottom wall vortex has a slightly greater strength than the upper and consequently produces a stagnation point above the centreline on the suction side.

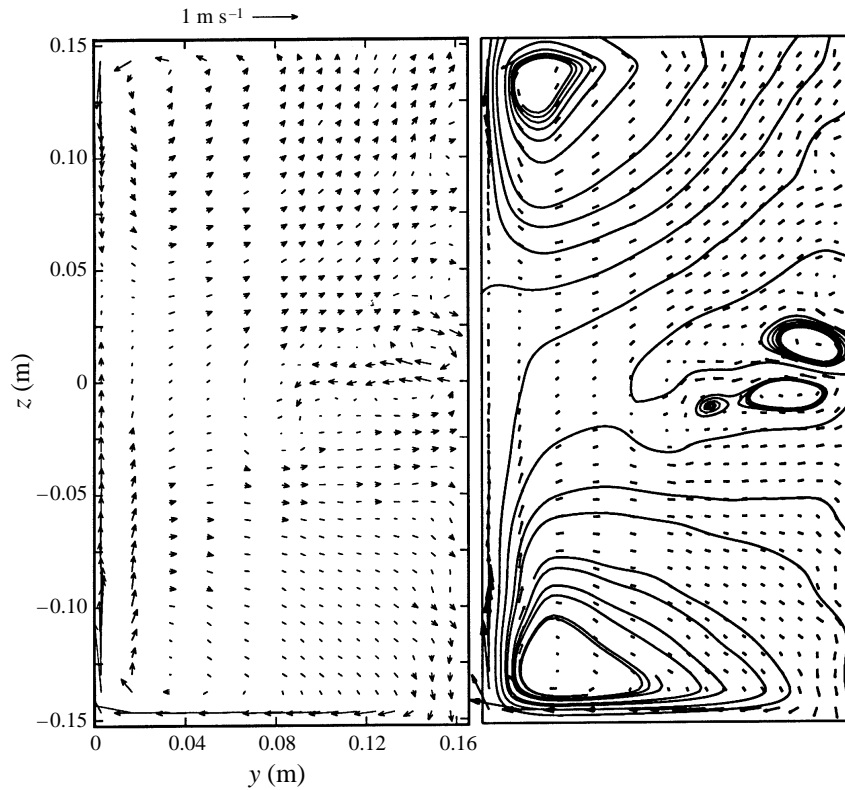


FIGURE 5. As figure 4 but at Station 4.

3.1.3. Cross-stream-plane results

Figures 2 to 7 show cross-stream-plane vector plots and corresponding integrated streamline patterns at stations 1 and 4 for $A = 1, 2$ and 4. The figures provide qualitative information regarding the effect of secondary flows on the mid-span boundary layer profiles.

For $A = 1$ (figures 2 and 3) the secondary flows are producing a significant extra strain rate (dW/dz) at station 1. For $A = 1$, station 4, the strongest secondary flow effect of all the measurements is seen.

For $A = 2$, figures 4 and 5 show the full duct, with $z = 0$ corresponding to the centreline. The influence of secondary flows at station 1 is negligible; the secondary flows are producing a weak extra strain rate (dW/dz) at station 4. For $A = 4$, the central region of the duct (around $z = 0$ at the top of the box in figures 6 and 7) shows negligible cross-stream velocity at stations 1 and 4.

It is apparent from the figures that a means of quantifying the strength of the secondary flows at the centreline is to evaluate $\partial W/\partial z$ and at least empirically determine a critical value of this velocity gradient that indicates when secondary flows will dominate the boundary layer development.

3.1.4. Secondary flow strength

The following analysis of secondary flows is not provided as a complete and rigorous answer to evaluating the importance of secondary flows. Rather it is an attempt to establish the important factors (at least in an order of magnitude sense) in determining the strength of secondary flow effects.

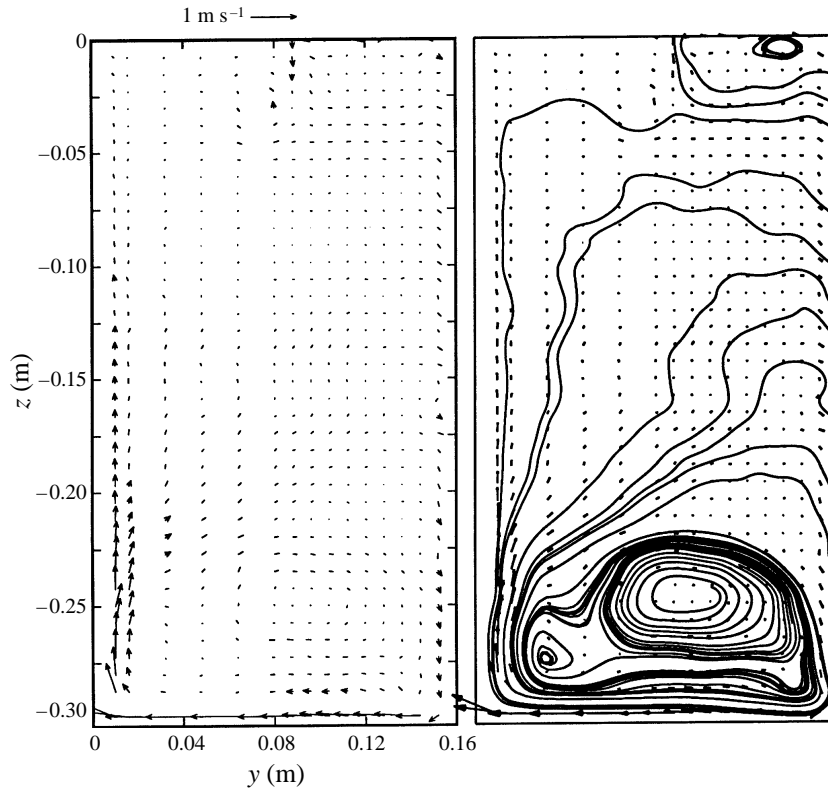


FIGURE 6. Mean cross-stream-plane vector field and streamlines. Station 1, $A = 4$. Flow out of page. Suction side at $y = 0$ as shown in figure 8.

Observations of some of the mid-span boundary layer mean-flow results presented in §3.2 below suggests that in some respects, the suction-side secondary flow effects are similar to that of an APG. Also, it appears that the suction-side results are more sensitive to secondary flows than those of the pressure side. This suggests that it is the more appropriate side to consider when trying to characterize the secondary flow strength. The suction-side effects would also be more important in terms of centrifugal machinery, where secondary flows and the subsequent reduction in skin friction may lead to earlier separation and stall of the centrifugal impeller.

APG flows are often characterized by Clauser's pressure gradient parameter β_x ($\beta_x = (\delta^*/\tau_0)(dP/dx)$). Following Panchapakesan *et al.* (1997) with their streamline convergence case, β_x was rearranged using Bernoulli's equation and continuity. The resulting 'divergence parameter' is given by

$$\beta_D = \frac{\delta^*}{U_\tau} S \frac{dW}{dz}, \quad (3.1)$$

where $S = U_e/U_\tau$ and δ^* is the displacement thickness. A number of similarities exist in the suction-side results affected by secondary flows (presented in §§3.2–3.4) and the streamline convergence case shown in Panchapakesan *et al.* (1997). The similarities are not surprising when one considers the centreline topology of the two flow cases. In both instances a streamwise saddle is observed along the centreline.

The cross-stream-plane measurements show clearly that when secondary flow effects

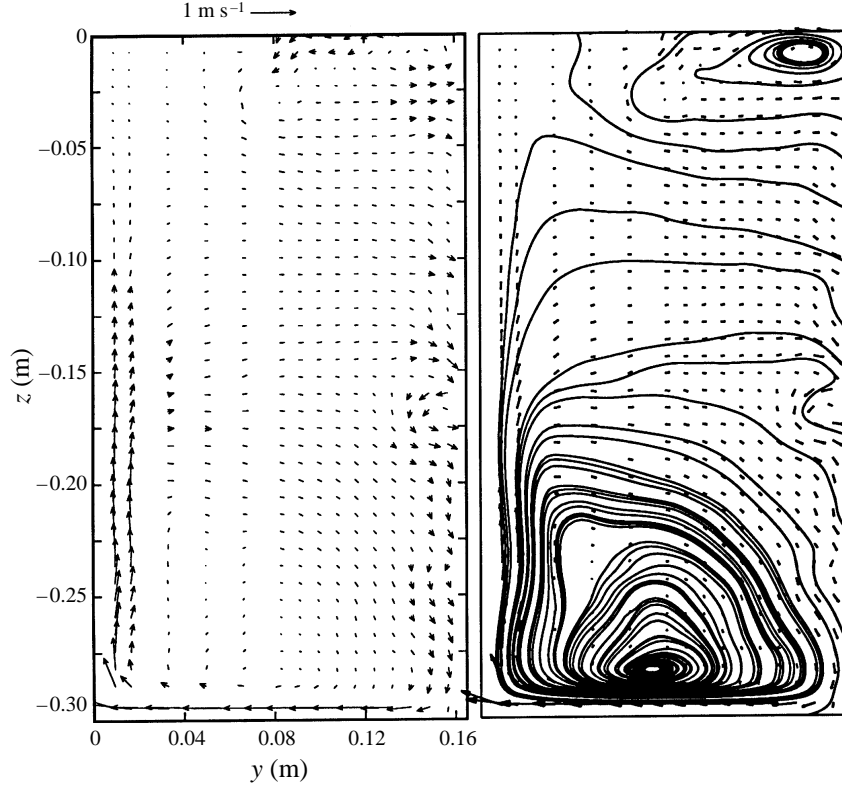


FIGURE 7. As figure 6 but at Station 4.

are apparent there is a significant velocity gradient, dW/dz . So an attempt will now be made to develop an expression for dW/dz in terms of the physical dimensions of the flow.

From the foregoing cross-stream-plane results it is obvious that a longitudinal vortex pair is generated on the walls perpendicular to the axis of rotation. Figure 8 is a schematic diagram of the cross-stream-plane flow, showing the way in which the flow was modelled and highlighting some of the assumptions used in the following analysis. They are:

(i) The pressure and suction-side wall boundary layers are small compared to the duct width b and as such may be ignored in terms of evaluating the pressure difference across the duct;

(ii) the boundary layers on the top and bottom walls of the duct (AB and CD) are uniform in the y -direction and have thickness δ ;

(iii) the top and bottom wall boundary layers develop similarly to the boundary layer measured on the stationary vertical wall.

The pressure gradient $\partial P^*/\partial y$ (generated by the Coriolis force) across the duct is given by

$$\frac{\partial P^*}{\partial y} = 2\pi\Omega U_e. \quad (3.2)$$

The above-mentioned assumptions leads to a pressure difference across the duct of

$$\Delta P^* = 2\rho\Omega U_e b, \quad (3.3)$$

where ρ is the fluid density, and U_e , b and h are as defined in figure 8.

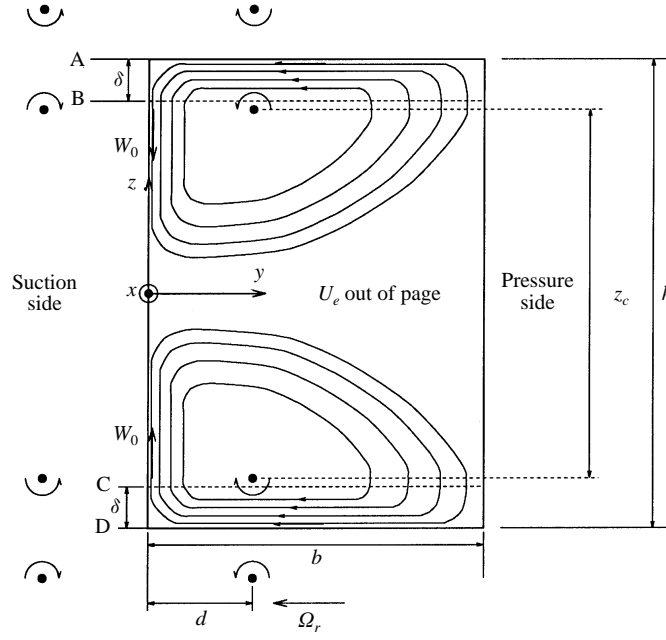


FIGURE 8. Schematic diagram of cross-stream flow pattern, flow out of page.

There were no vertical forces acting on the fluid at the top and bottom boundaries of the duct, so the static pressure remains constant over the full height of the pressure and suction sidewalls. Over most of the duct the force generated by the pressure variation ΔP^* is balanced by the Coriolis force. However, within the top and bottom wall boundary layers the Coriolis force is reduced due to the reduction in streamwise velocity U . So a net force is generated on the fluid (F_1), which for one of the boundary layers can be approximated by

$$F_1 = 2\Omega U_e \rho b \delta - \int_0^\delta 2\Omega U \rho b dz = 2\Omega \rho b \int_0^\delta (U_e - U) dz = 2\Omega \rho b U_e \delta^*. \quad (3.4)$$

For the zero-pressure-gradient stationary case, δ^* can be approximated by a linear function in x , see figure 9 (discussion and details are given in §3.2.6). Non-dimensionalizing δ^* using duct width b then gives

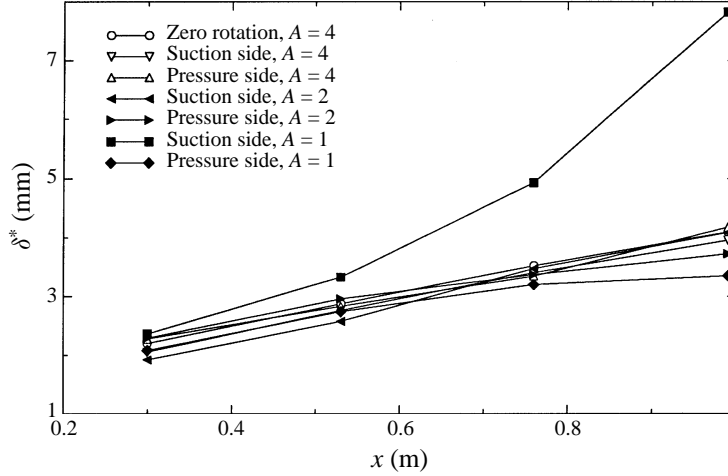
$$\frac{\delta^*}{b} = B_1 \xi + \frac{\delta_0}{b}, \quad (3.5)$$

where $\xi = x/b$. The constants were determined from figure 9, the stationary case, and were $B_1 = 0.0027$ and $\delta_0 = 0.0014$. F_1 becomes

$$F_1 = 2\Omega \rho b^2 U_e \left(B_1 \xi + \frac{\delta_0}{b} \right). \quad (3.6)$$

The force, F_1 was assumed to be balanced by the impulse from the vortex pair (F_2) given by

$$F_2 = \rho \frac{d\Gamma}{dt} z_c, \quad (3.7)$$

FIGURE 9. Displacement thickness versus x .

where Γ is the vortex circulation. The distance z_c was difficult to ascertain with certainty from the cross-stream-plane plots; however, for a first approximation, assume z_c scales with the height of the duct, so $z_c = B_2 h$ and $dt = dx/U_e$, so

$$F_2 = \rho \frac{d\Gamma}{dx} U_e B_2 h. \quad (3.8)$$

Estimation of B_2 from the cross-stream-plane plots gave $B_2 = 0.68$.

Equating $2F_1$ (top and bottom pressure imbalance) and F_2 (vortex impulse) gives

$$\frac{d\Gamma}{dx} = \frac{4\Omega b}{B_2 A_s} \left(B_1 \xi + \frac{\delta_0}{b} \right), \quad (3.9)$$

where $A_s = h/b$ is the aspect ratio of the duct. Substituting for x and integrating gives

$$\Gamma = \frac{4\Omega b^2}{B_2 A_s} \left(\frac{B_1}{2} \xi^2 + \frac{\delta_0}{b} \xi + B_3 \right). \quad (3.10)$$

The constant of integration was evaluated by assuming that $\Gamma = 0$ at the 'effective origin' ($\xi|_{\delta^*=0}$), as defined by equation (3.5). This gives an expression for the constant

$$B_3 = \frac{\delta_0^2}{2b^2 B_1}. \quad (3.11)$$

For the current study, $B_3 = 0.014$.

The suction sidewall was then modelled with the system of image vortices shown in figure 8. A complex potential expression (ω) for the system of vortices was evaluated. The expression is

$$\omega = \sum_{j=1}^8 -\frac{i\Gamma}{2\pi} \ln(z_1 - (y_j + iz_j)), \quad (3.12)$$

where $z_1 = y + iz$ and (y_j, z_j) are the centre locations of the point vortices defined by the constant B_2 previously mentioned and $d = 0.25b$ estimated from the cross-stream-plane measurements. Differentiation of this expression gives the velocity field (i.e.

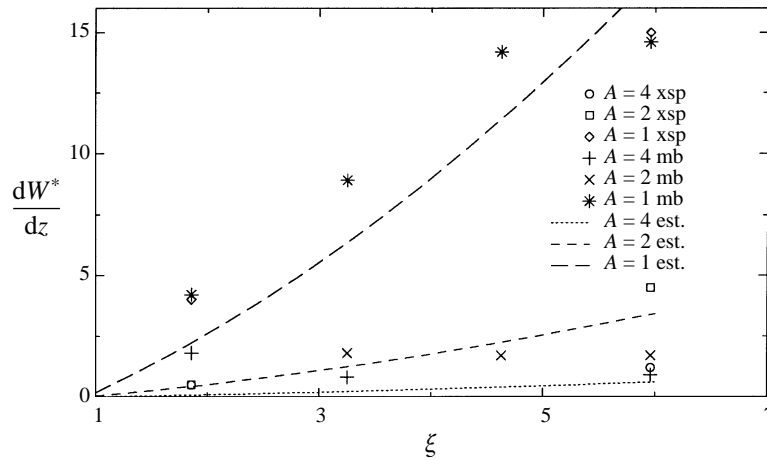


FIGURE 10. Measured values of dW/dz compared with estimates from analysis. Note, in the figure legend 'xsp' means dW/dz was evaluated from cross-stream-plane results and 'mb' means dW/dz was evaluated from the momentum balance results

$V + iW = d\omega/dz_1$). The W velocity field expression was differentiated with respect to z . The resulting expression was then used to evaluate dW/dz at the suction-side centreline ($y = z = 0$). The values of dW/dz are shown in figure 10.

The dW/dz values obtained from the cross-stream-plane measurements were checked with a second estimate obtained from the momentum integral, equation (3.15) below. The estimate of $d\theta/dx$ was obtained from a curve fit to the suction-side profiles of θ versus x shown in figure 11. The remaining terms in the equation were evaluated from the mean-flow profiles, as explained in §3.2.2.

The measured values of dW/dz and the estimates from the above analysis show reasonable agreement, at least in terms of the general trends. There was some scatter in the estimates of dW/dz particularly where the secondary flows were weak, which was to be expected since the magnitude of dW/dz was small resulting in significant error. Where secondary flows are strong the agreement was improved.

The technique obviously requires more rigorous testing before it could be said that it is generally useful. However, it appears to have some merit for evaluation of secondary flow strength, at least in zero-pressure-gradient rotating ducts or blade passages where the aspect ratio is approximately constant with x .

Bradshaw (1973) described flows with streamline convergence as mildly perturbed when the ratio $B = (\partial W/\partial z)/(\partial U/\partial y) < 0.1$. When $B > 0.1$ the flow was described as strongly perturbed. The ratio B was evaluated at $y/\delta = 0.5$ and the results for the current study are shown in figure 12, which shows that the flow is approaching Bradshaw's criterion of strongly perturbed for $A = 1$ station 4. There are a number of reasons for re-defining strongly perturbed. Firstly, Bradshaw's parameter was suggested for flows with streamline divergence which usually had some development length prior to the application of the extra strain rate. The prior development of the boundary layer resulted in reduced wall normal velocity gradients ($\partial U/\partial y$) and consequently larger value of B . Secondly, the additional Coriolis effect in the current study may result in the $\partial W/\partial z$ gradient influencing the boundary differently to the stationary case discussed by Bradshaw.

The boundary layer measurements presented in §§3.2 and 3.3 show that significant secondary flow effects are seen at $A = 1$, station 3. This corresponds to $B \simeq 0.07$ or

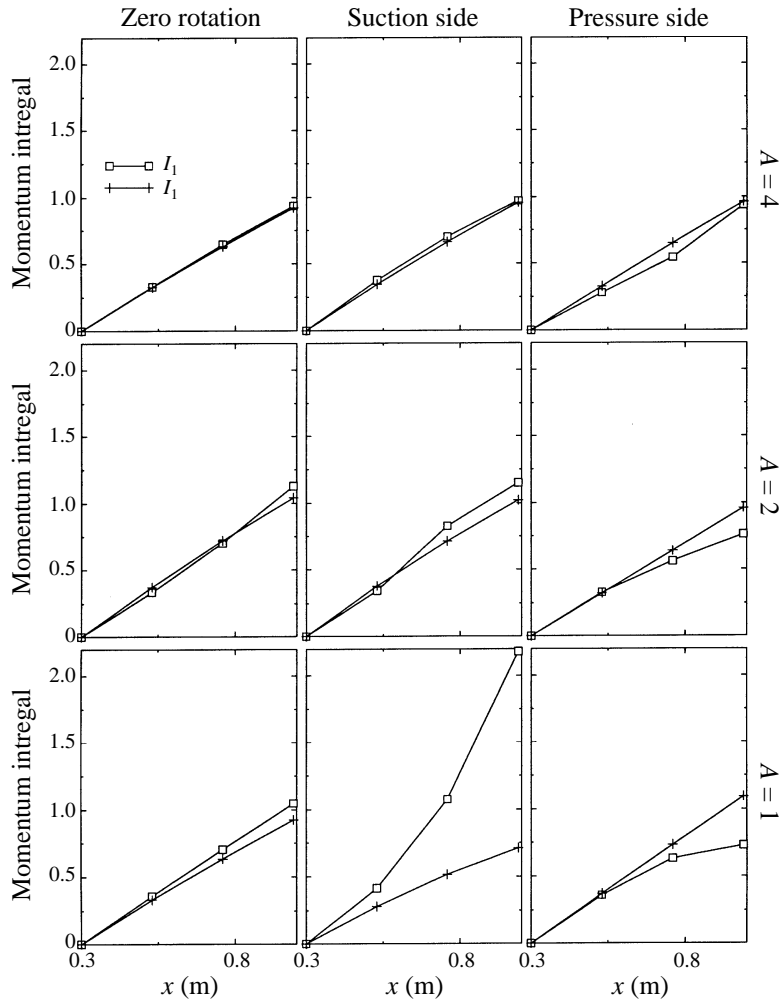


FIGURE 11. Momentum balance profiles for all cases where $I_1 = (\theta - \theta_0)/\theta_0$ and $I_2 = (1/2\theta_0) \int_{x_0}^x C_f' dx$.

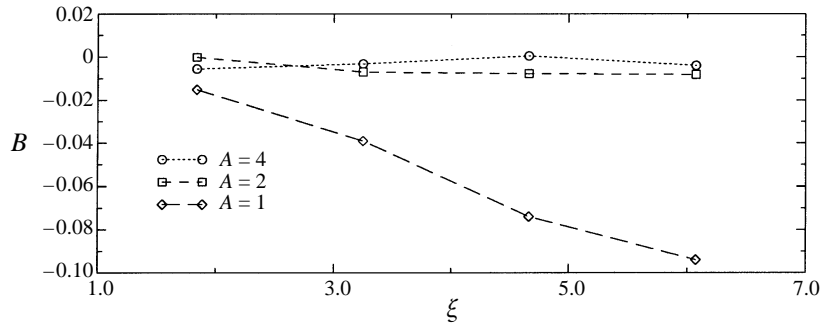


FIGURE 12. Bradshaw's divergence parameter B versus ξ , evaluated at $y/\delta = 0.5$.

	Station 1	Station 2	Station 3	Station 4
$A = 4$	0.17	0.12	0.02	0.22
$A = 2$	0.01	0.23	0.33	0.42
$A = 1$	0.49	1.69	4.61	10.00

TABLE 1. β_D for all suction-side boundary layers. Note the estimate of dW/dz used to evaluate β_D was that obtained from the momentum balance profiles.

$\beta_D = 4.6$. Therefore, it is concluded that $\beta_D > 4.6$ represents a case dominated by secondary flows. Values of β_D for all suction-side boundary layers are given in table 1.

3.2. Mean-flow results and discussion

A substantial amount of mean-flow data were taken in the tunnel for the rotation conditions outlined in §2.

The mean-flow results were measured with both Pitot tubes and normal hot-wire anemometers. In most cases the results of the two methods agreed to better than 2%. Obviously each method has associated uncertainties, especially in the rotating cases where static pressure varied across the duct. It was felt that the Pitot tube results represented the more accurate set of data so these results have been used for the data that follow in this section.

3.2.1. Presentation of data

Boundary layer mean velocity and turbulence measurements showed little variation between the $A = 4$ and $A = 2$ cases. In order to minimize the number of figures, profiles shown here are limited to stations 1 and 4, $A = 1$ and $A = 2$. Data evaluated from profiles (such as boundary layer thickness, displacement thickness, etc.) have been shown for all aspect ratios and measurement stations. Complete data sets can be found in Macfarlane (1997).

3.2.2. Boundary layer momentum balance

The momentum integral equation for a turbulent boundary layer developing in a zero pressure gradient with system rotation is

$$\frac{d\theta}{dx} = \frac{C'_f}{2}, \quad (3.13)$$

which is unchanged from the non-rotating case. Further discussion of θ is given in §3.2.6. If we consider the low-aspect-ratio cases where the secondary flow generates an extra rate of strain dW/dz (refer to §3.1) then an alternative form of the momentum integral equation must be considered.

Kehl (1943) and Head & Patel (1970) evaluated the momentum equation on the plane of symmetry, for flows with simple, lateral divergence or convergence. In their case ‘simple’ meant dW/dz was constant throughout the layer. This might not be strictly true in the current flow case; however it was assumed to apply here. As previously discussed, the suction-side behaviour resembles that of simple streamwise convergence. Their momentum equation was

$$\frac{d\theta}{dx} = \frac{C'_f}{2} - (H+2) \frac{\theta}{U_e} \frac{dU_e}{dx} - D\theta, \quad (3.14)$$

where $D = (1/U_e)/(dW/dz)$.

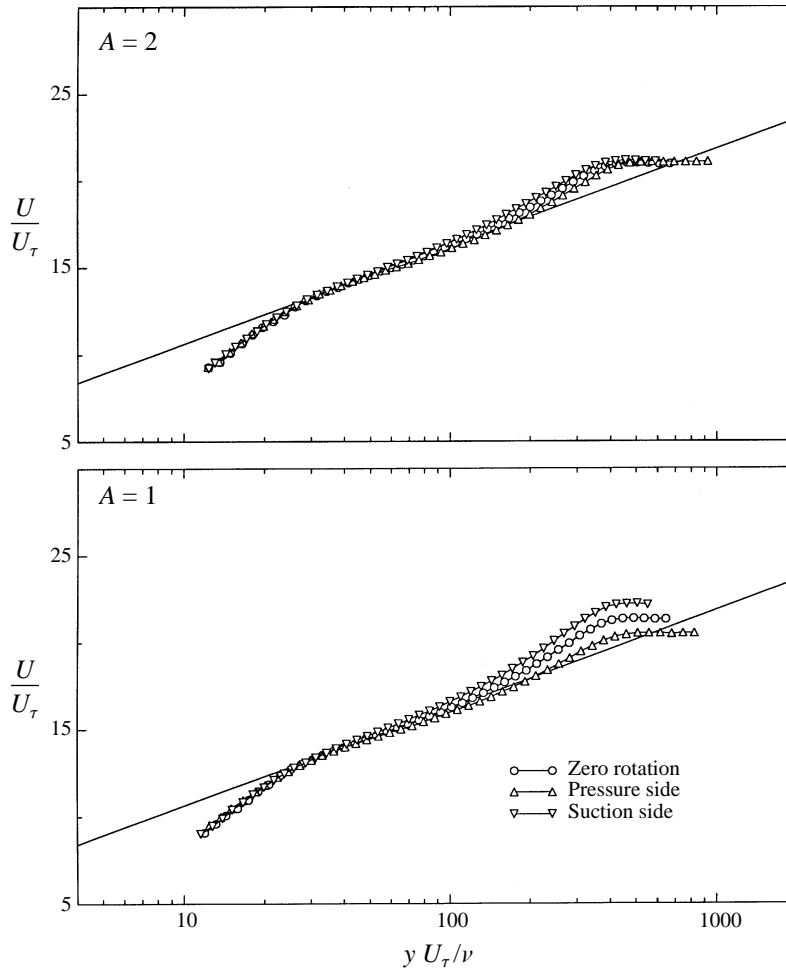


FIGURE 13. Station 1 centreline mean velocity profiles, U/U_τ vs. yU_τ/ν ; aspect ratio as marked.

Nickels & Joubert (1997) used equation (3.14) in discussion of possible equilibrium solutions of the boundary layer equations with lateral straining. Following their analysis we substitute the divergence parameter β_D (as given in equation (3.1)), the Clauser pressure gradient parameter β_x (as given in §3.1.4)), the shape factor $H = \delta^*/\theta$, and define $S = U_1/U_\tau$. After some manipulation and substitution of the zero-pressure-gradient case ($\beta_x = 0$) equation (3.14) reduces to

$$\frac{d\theta}{dx} = \frac{C'_f}{2} \left[1 + \frac{\beta_D}{H} \right]. \quad (3.15)$$

The interpretation of equation (3.15) is that if we plot $d\theta/dx$ versus x and $C'_f/2$ versus x , then when the two curves collapse, the β_D/H term is negligible. This indicates the secondary flow effect is negligible. When the curves diverge, secondary flow effects are present, and the difference can be used to evaluate the divergence parameter β_D . The dW/dz results (extracted from β_D calculated in this way) are shown in figure 10.

Evaluation of $d\theta/dx$ in equation (3.13) involves curve fitting experimental points to obtain an estimate of $d\theta/dx$. This procedure often introduces inaccuracies so an

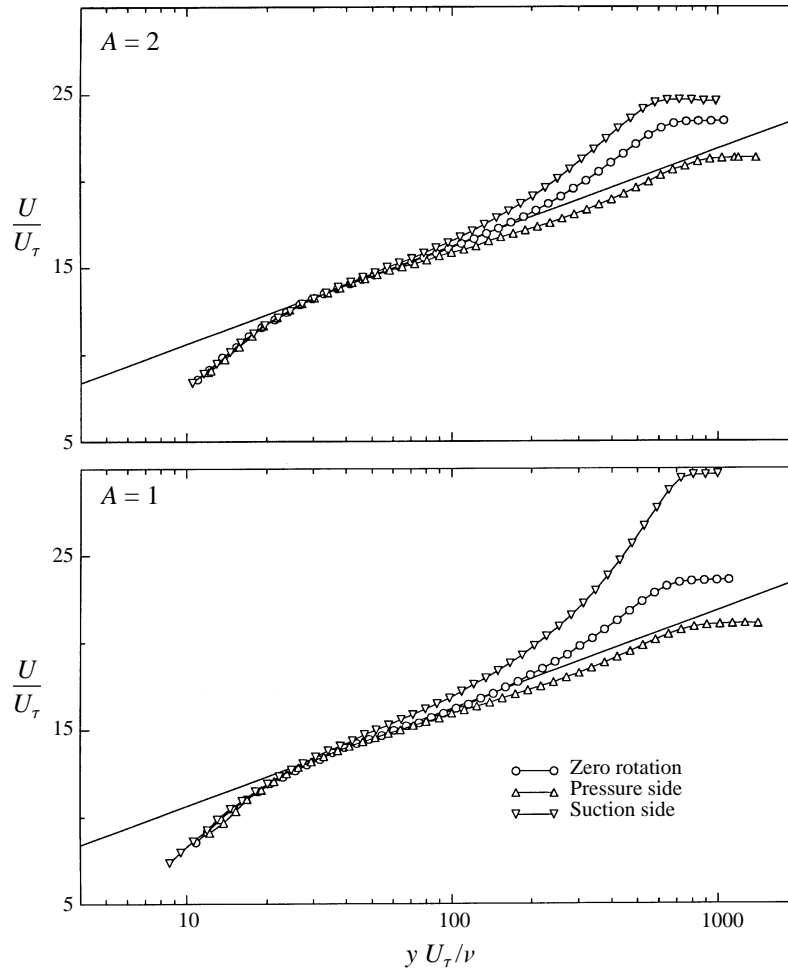


FIGURE 14. As figure 13 but at Station 4.

alternative method was used. Following Erm & Joubert (1991) equation (3.13) was integrated giving

$$\frac{\theta - \theta_0}{\theta_0} = \frac{1}{2\theta_0} \int_{x_0}^x C_f' dx. \quad (3.16)$$

Both sides of this equation were directly evaluated from the experimental data profiles and compared at each streamwise location. The '0' subscript here refers to the most upstream station where measurements were taken.

The momentum balances were shown in figure 11. As expected the $A = 4$ momentum balances are good for all rotation conditions. The zero rotation balance is within 2% for all measurement stations and the rotating cases are generally within 6%. The lower-aspect-ratio flow cases studied show a reasonable balance for zero rotation, but with rotation, the balance is poor. This is to be expected from the effects of secondary flows depositing fluid in the suction-side boundary layer and removing it from the pressure side.

This also confirms that the boundary layer profiles developing in the non-rotating ducts were 'normal' and that the $A = 4$ case is unaffected by secondary flows for the

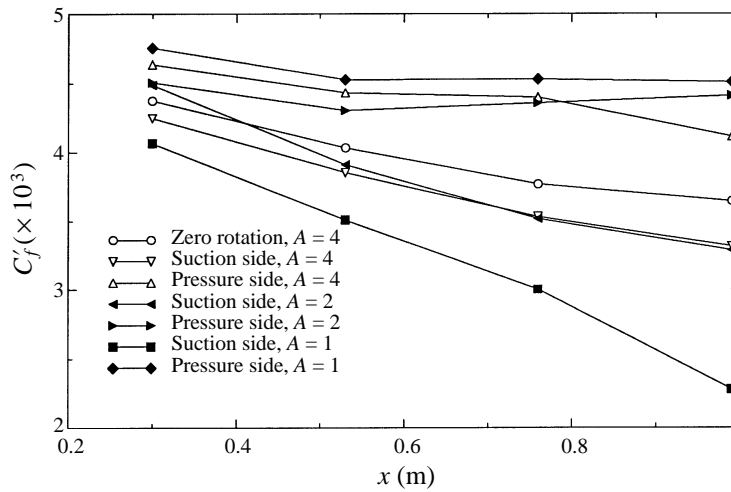


FIGURE 15. Streamwise skin friction variation.

measured stations, while the secondary flow effects are seen to increase with increasing streamwise distance x and reducing aspect ratio.

3.2.3. Mean flow profiles and the logarithmic law of the wall

Figures 13 and 14 show the mean-flow profiles in conventional ‘law of the wall’ coordinates. As found by previous workers (see Watmuff *et al.* 1985) in rotating flows, the gradient of the logarithmic region was modified with rotation. The pressure-side gradient was reduced and the suction-side one increased. Secondary flows did not significantly alter the variation of the gradient.

3.2.4. Skin friction

Figure 15 shows the streamwise skin friction distribution. The zero-rotation skin friction results were similar in all cases, so to reduce congestion in the figure the only zero-rotation result shown is for $A = 4$. The plot clearly shows the strong influence of the Ekman layer on the boundary layer for $A = 1$ with a marked reduction in skin friction on the suction side. The reduction in skin friction on the suction side was also seen in the APG flow case presented in Macfarlane & Joubert (1992). They suggest that low-aspect-ratio rotating diffusing flows would be more susceptible to separation or stall than higher aspect-ratio cases in an otherwise equivalent flow. The differences on the pressure side are much smaller. At station 4 a small increase in the skin friction is seen as aspect ratio is reduced.

Spanwise skin friction results presented in Macfarlane & Joubert (1995) suggested that the pressure-side roll cell pattern was little affected by secondary flows.

3.2.5. Boundary layer thickness

The definition of boundary layer thickness (δ) used in the current investigation is $\delta = y|_{U/V_\infty=0.995}$. Boundary layer growth is shown in figure 16. As for figure 15, the only zero rotation case shown is for $A = 4$. The expected trend of growth promoted on the pressure side and suppressed on the suction side, due to the influence of the Coriolis instability alone, is seen for $A = 4$. The $A = 2$ case shows similar results with very little effect of Ekman layers on the mid-span mean flow profiles. The $A = 1$ case shows significant effects of the Ekman layer. Initially the suction- and pressure-side layers are

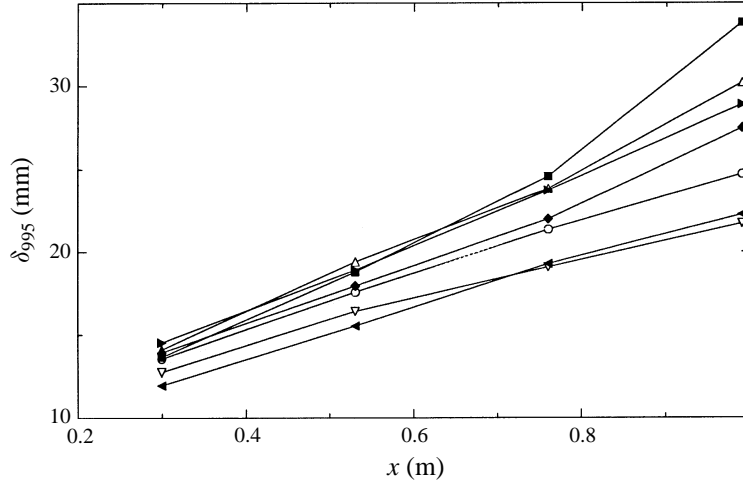


FIGURE 16. Boundary layer thickness versus streamwise distance, δ_{995} vs. x . Symbols as figure 15.

almost equal in thickness and both slightly thicker than for zero rotation. Both layers thicken more rapidly than the zero-rotation case with the suction side growing more rapidly than the pressure side.

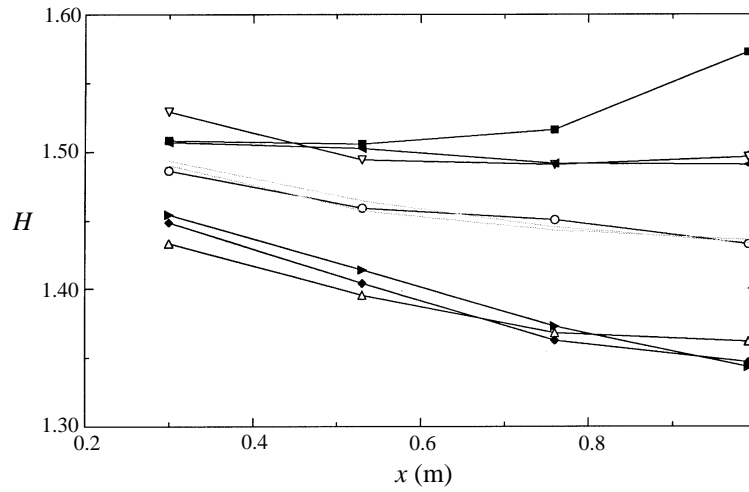
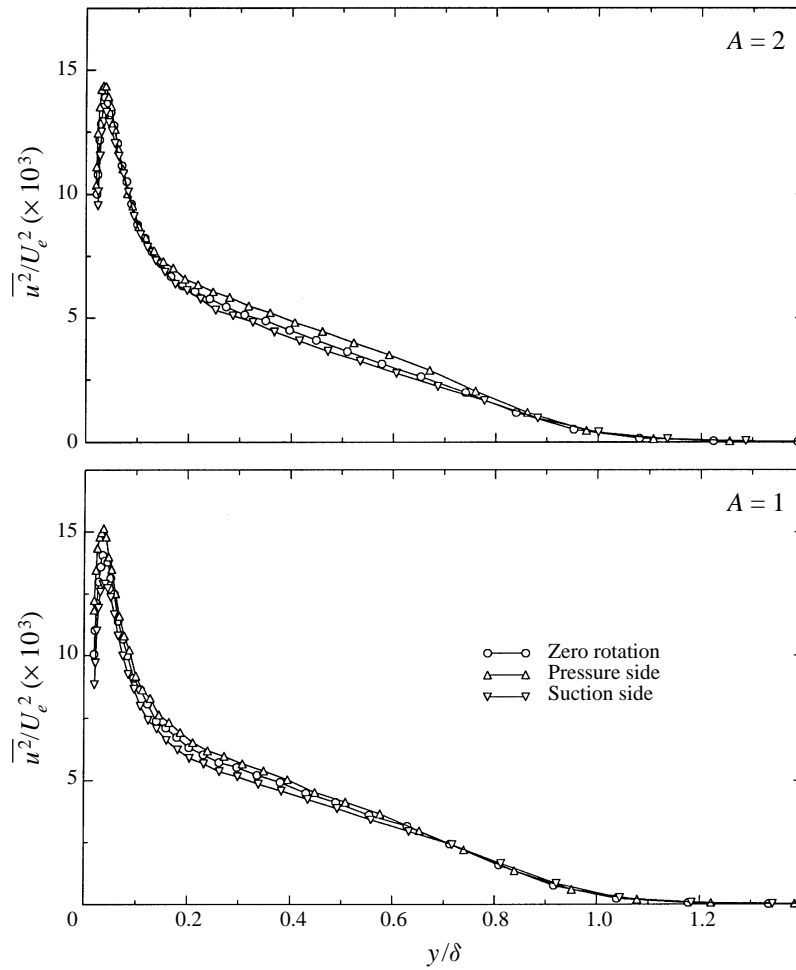
3.2.6. Boundary layer integral parameters

The displacement thickness δ^* and momentum thickness θ were defined in the usual way and the shape parameter H was defined as $H = \delta^*/\theta$.

Profiles of displacement thickness were shown in figure 9. The deviation from the zero-rotation curves is small in all cases except for the $A = 1$ suction-side profile. The $A = 4$ pressure-side profiles show a small increase in δ^* over the range of x values measured and the suction-side ones show a small decrease, relative to the zero-rotation case. The $A = 2$ profiles show initially the same trends with rotation as the $A = 4$ case; however, at station 4 the pressure side has reduced to below the zero-rotation case. The $A = 1$ case pressure side is entirely below the zero rotation curve, opposite to the higher-aspect-ratio case. The $A = 1$ suction-side values of δ^* are all significantly above the zero-rotation case and increase rapidly with streamwise development.

The θ versus x profiles (not shown here) show similar trends to the δ^* profiles for all cases. The magnitude of variations with rotation at each aspect ratio are slightly greater. The small variations in θ and δ^* are to be expected since the Coriolis force is always approximately normal to the mean flow and hence cannot directly affect these measures. The significant variation seen in the $A = 1$ case must be due to the dW/dz velocity gradient.

The shape parameter, H , plotted in figure 17, shows clear trends for all rotation cases, although the magnitude of the variation is small. The maximum variation is approximately 6% in all but the $A = 1$ suction-side case. In that case the maximum variation is 10%. The zero-rotation profiles show good agreement with each other. Pressure-side profiles are reduced and suction-side profiles increased, relative to the zero-rotation case. The $A = 1$ suction-side profile increased more rapidly with streamwise development than the lower-aspect-ratio suction-side profiles.

FIGURE 17. Shape parameter, H , versus x . Symbols as figure 15.FIGURE 18. Station 1 streamwise turbulence intensities, $\overline{u^2}/U_e^2$ vs. y/δ ; aspect ratio as marked.

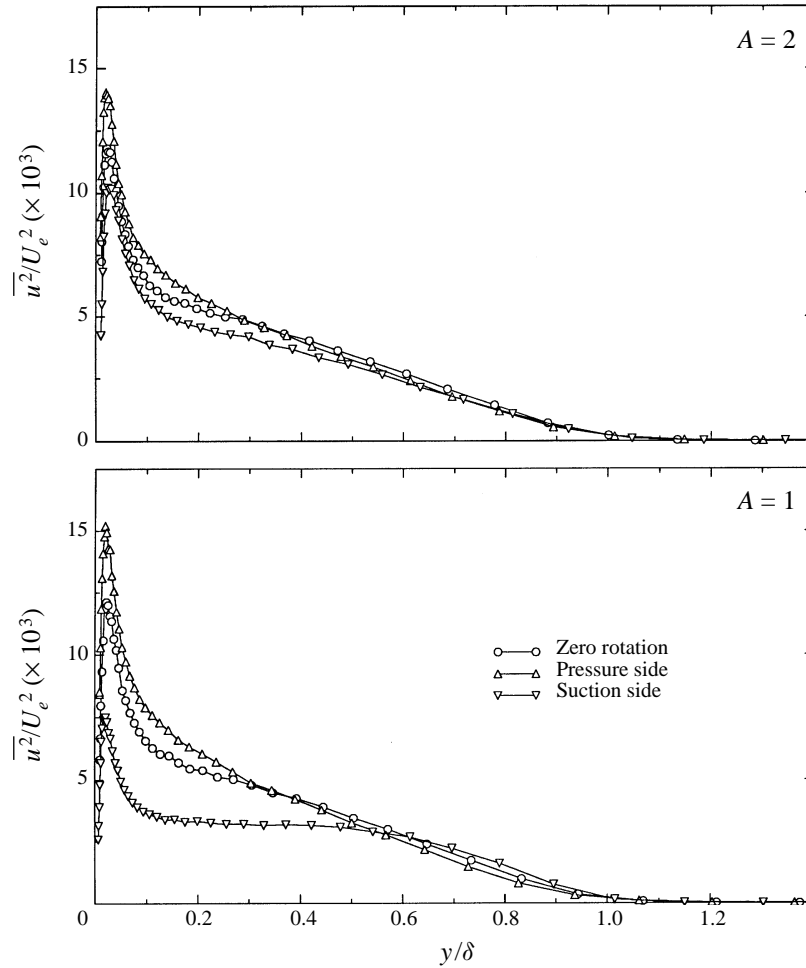


FIGURE 19. As figure 18 but at Station 4.

3.3. Broadband turbulence, results and discussion

In this section broadband turbulence results are presented. A substantial amount of turbulence data were taken in the tunnel for the experimental conditions outlined in §2. Turbulence results are presented for boundary layers subject to Coriolis force alone ($A = 2$) and then combined Coriolis force and secondary flow effects ($A = 1$).

The u -component turbulence results were measured with a normal wire and other results were measured with the cross-wire in either ' uw ' or ' uw' ' mode. The results include Reynolds normal and shear stresses.

3.3.1. Profiles of $\overline{u^2}$

Figures 18 and 19 show profiles of $\overline{u^2}/U_e^2$ versus y/δ . Rotation enhances the magnitude of the streamwise component of normal stress on the pressure side and suppresses the component on the suction side. The rotation term in equation (1.2) suggests that the effect should be opposite to that observed. The indirect effect of the shear stress term must dominate the development of the $\overline{u^2}$ term.

Previous workers (e.g. Erm 1988; note that substantial portion of his results have been published in the open literature in Erm & Joubert 1991) have also found that

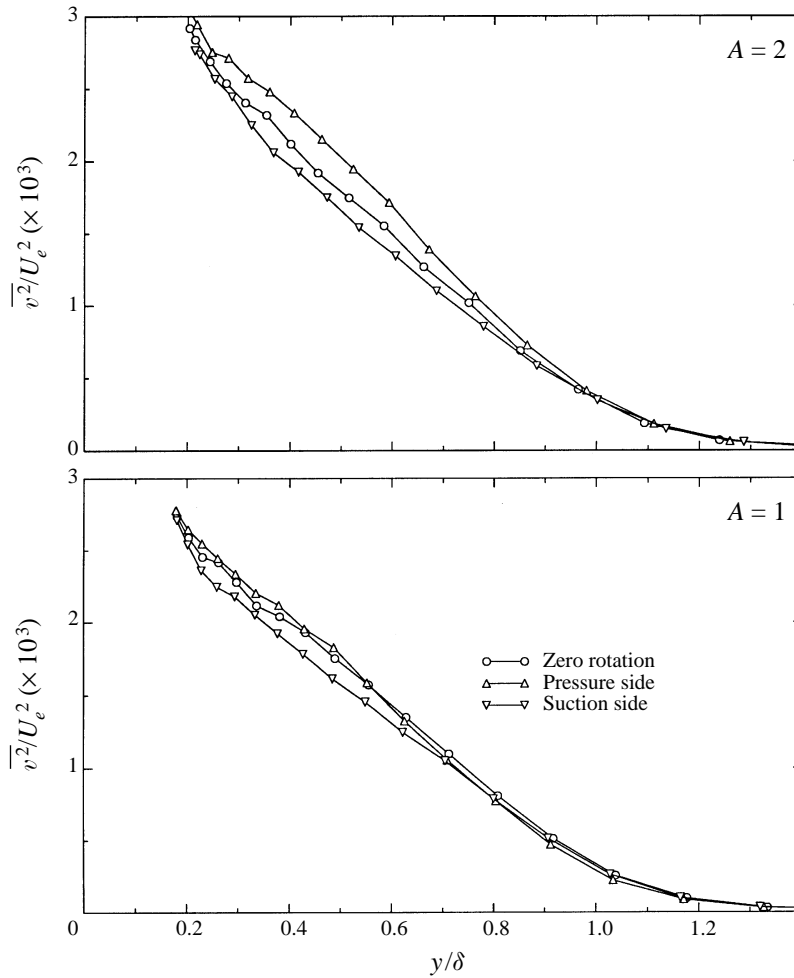


FIGURE 20. Station 1 wall normal turbulence intensities, $\overline{v^2}/U_e^2$ vs. y/δ ; aspect ratio as marked.

profiles plotted with this scaling show an independence from R_θ for y/δ greater than 0.3 and R_θ greater than 1000. When $y/\delta < 0.3$, increasing R_θ decreases the magnitude of stresses. One could argue from these results that pressure-side rotation appears to behave similarly to a reduction in development length and suction-side rotation corresponds to an increase in development length. This is opposite to the appearance given when the semi-logarithmic wall scaling was used, with U_τ and ν used as scaling parameters, as has been shown by Macfarlane & Joubert (1998). Similar results can be shown for the other components of normal stresses.

3.3.2. Profiles of $\overline{v^2}$

The $\overline{v^2}$ and $\overline{w^2}$ components of normal stresses were measured with a cross-wire. Limitations of the cross-wire probe geometry prevented measurements close to the wall. Details such as the peak observed in stresses with the normal-wire measurements at $y/\delta = 0.02$, cannot be seen with the cross-wire results.

Figures 20 and 21 show the profiles of $\overline{v^2}/U_e^2$ versus y/δ . Although there is only a small amount of data in this region, the $A = 2$ profiles close to the wall ($y/\delta < 0.2$)

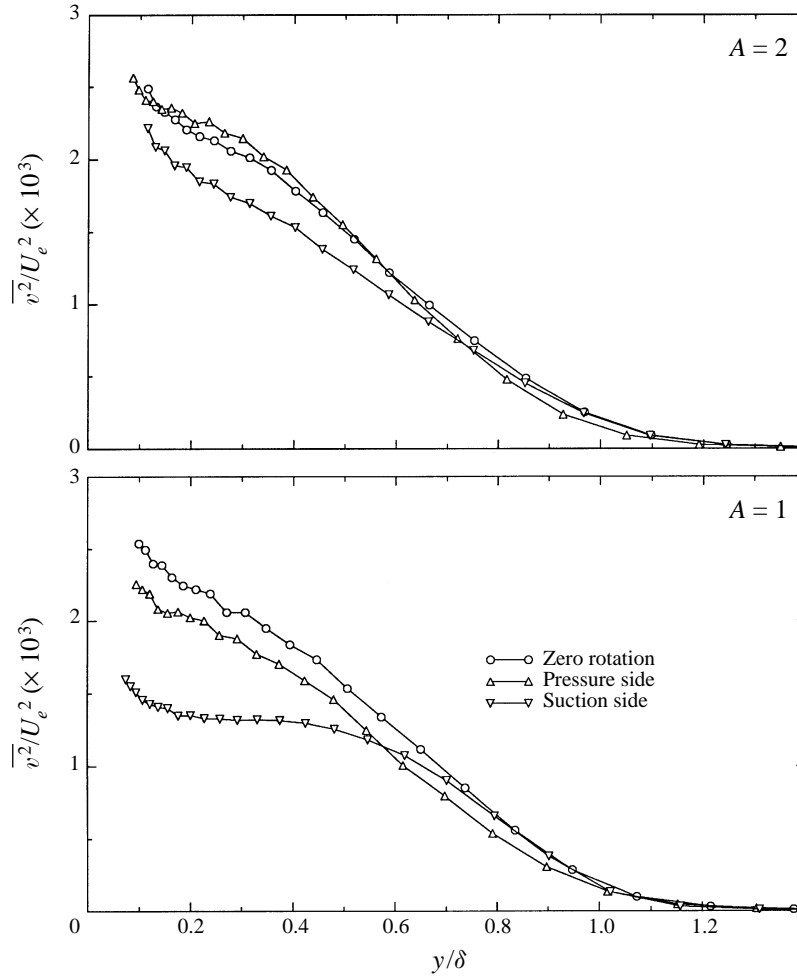


FIGURE 21. As figure 20 but at Station 4.

seem to converge. The results show an enhancement on the pressure side and a suppression on the suction side for $0.2 < y/\delta < 0.9$, as anticipated from equation (1.3). This equation contains the production term $+2\omega\bar{w}\bar{v}$ suggesting an increase in \bar{v}^2 on the pressure side and a decrease in the suction side for the two-dimensional flow of the $A = 2$ case. The y/δ range of enhancement/suppression reduces with increasing x . The pressure-side enhancement for $A = 1$ is offset by the secondary flow effects and the profiles for the first three stations deviate little from the zero-rotation case. The $A = 1$ suction-side layers remain suppressed relative to the zero-rotation case and with streamwise development (increasing secondary flow strength) the suppression near the wall increases significantly. The profiles appear similar to the streamline convergence case in Hafez (1991).

3.3.3. Profiles of \bar{w}^2

Figures 22 and 23 show the profiles of \bar{w}^2/U_e^2 versus y/δ . This component of stress seems little affected by Coriolis forces, as would be expected from equation (1.4). The $A = 2$ profiles show only a slight suppression/enhancement on the suction/pressure

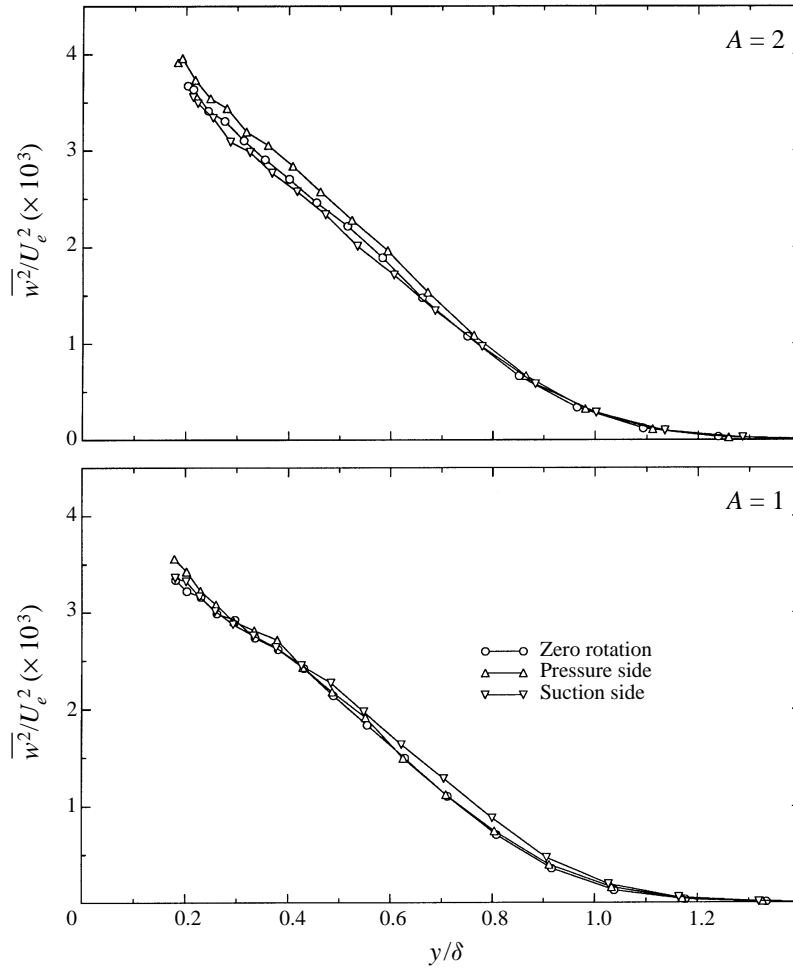


FIGURE 22. Station 1 spanwise turbulence intensities, $\overline{w^2}/U_e^2$ vs. y/δ ; aspect ratio as marked.

side. The case with strong secondary flow effects ($A = 1$, station 4) shows a large reduction in the magnitude of $\overline{w^2}$ near the wall. Again this is a similar profile to that shown in Hafez (1991) for the streamline convergence case and can be anticipated from equation (1.4).

3.3.4. Reynolds shear stress

Reynolds shear stress profiles \overline{uw}/U_e^2 vs. y/δ are shown in figures 24 and 25. As for the normal components, the shear stresses of the $A = 2$ pressure side have been enhanced relative to the zero-rotation case and suppressed on the suction side. For $A = 1$ similar trends to those observed in the normal stresses are also observed. The $A = 1$ pressure-side layers have been reduced to be only slightly above the zero-rotation case for station 1. At station 4, where secondary flows are strongest (dW/dz greatest) the stresses on the pressure side are reduced below the stationary case. The stresses in the suction-side layers at $A = 1$, station 4, have been significantly reduced close to the wall, similar to the trends shown in Hafez (1991) for the streamline convergence case.

The \overline{uw} vs. y/δ profiles should be zero for a two-dimensional non-rotating boundary

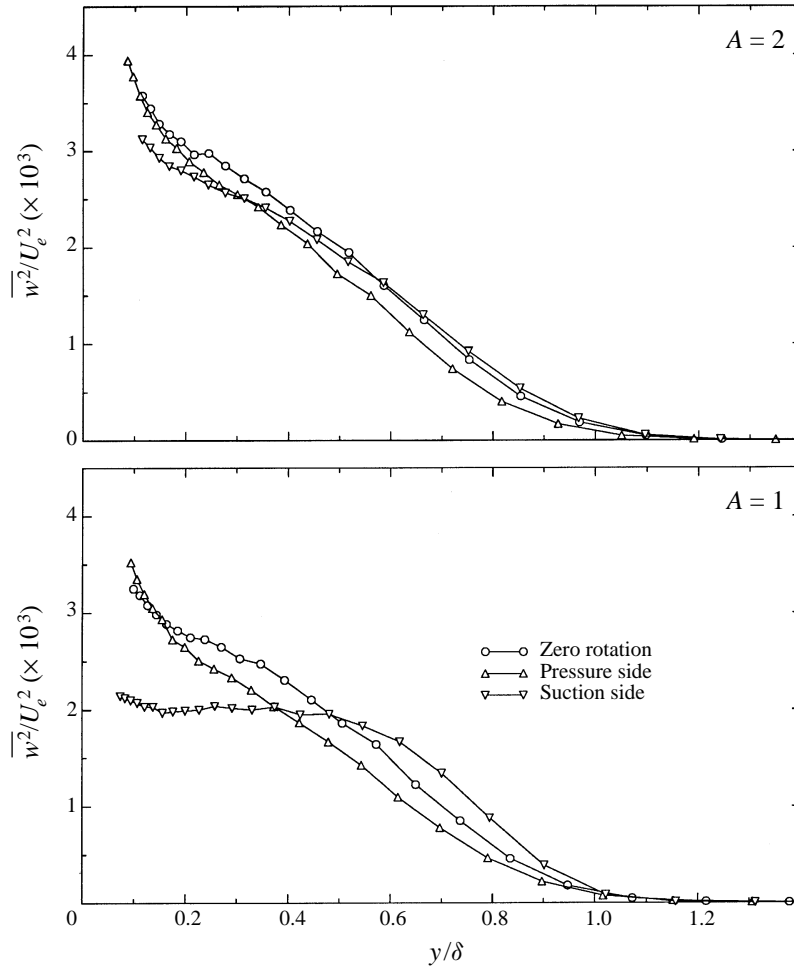


FIGURE 23. As figure 22 but at Station 4.

layer. These profiles were plotted to investigate the effect of rotation and secondary flows. The profiles showed little variation with streamwise development, so only the station 4 results are shown, in figure 26. The zero-rotation and suction-side results are nearly one order of magnitude smaller than the \overline{uw} results for $y/\delta > 0.2$. For all aspect ratios the suction-side results differ little from the zero rotation case and are close to zero for $y/\delta > 0.2$. The $A = 2$ pressure-side results are significantly enhanced relative to the zero-rotation case for $y/\delta < 0.8$. The $A = 1$ pressure-side profile is only slightly above the zero rotation case. The enhancement of the pressure-side centreline \overline{uw} measurement is probably due to the action of the longitudinal roll cell pattern. All profiles rise quite sharply for $y/\delta < 0.2$ and this can probably be attributed to shear across the cross-wire sensing elements in the 'uw' mode, rather than a physical increase in the magnitude of this quantity.

The Reynolds stress results demonstrate clearly that the effects of Coriolis forces are being overwhelmed by the secondary flow effects for the $A = 1$ case by station 3.

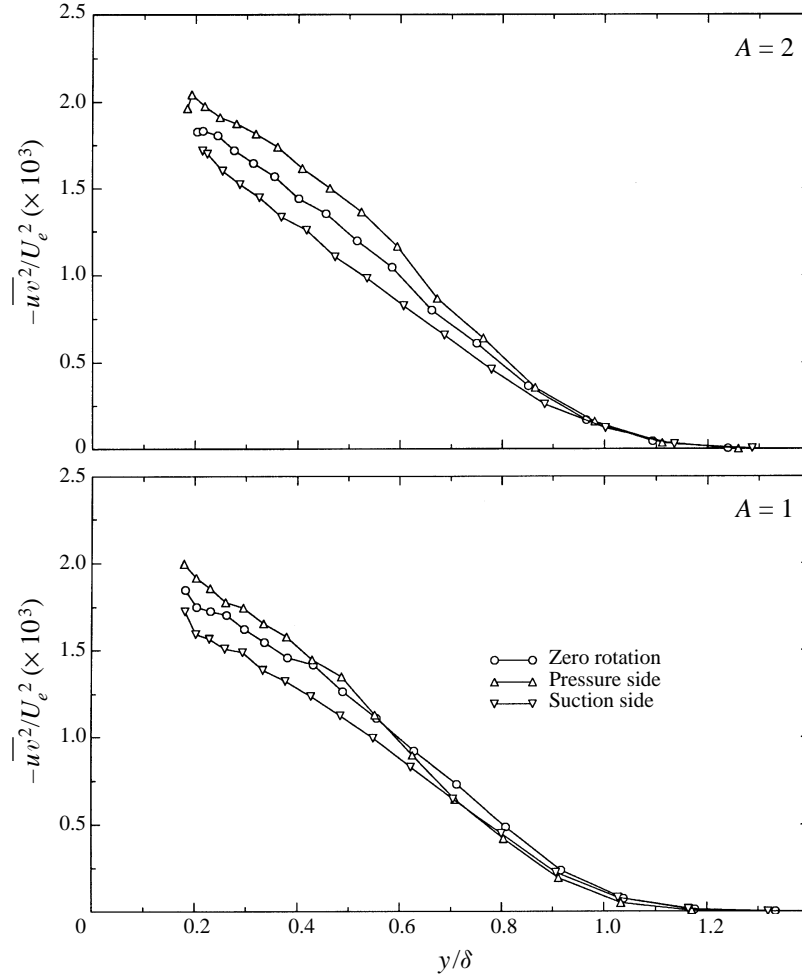


FIGURE 24. Station 1 Reynolds shear stress, $-\overline{uv}^2/U_e^2$ vs. y/δ ; aspect ratio as marked.

3.4. Spectra results and discussion

In this section a limited selection of spectra results are presented and analysed. The measurement techniques were outlined in §2. The results presented are for boundary layers subject to Coriolis force alone ($A = 2$) and combined Coriolis force and secondary flow effects ($A = 1$).

3.4.1. Previous work

A number of previous studies have been presented using the scaling laws of Perry, Henbest & Chong (1986) for both low-Reynolds-number boundary layers and some work where the boundary layer was subjected to rotation. Erm (1988) presented a detailed study of low-Reynolds-number boundary layers and how various tripping devices affected the spectra. Watmuff *et al.* (1985) presented a small number of spectra profiles demonstrating the effect of Coriolis forces. Ibal (1990) presented a detailed study of how the combined effects of low Reynolds number, APG and rotation affected boundary layer spectra.

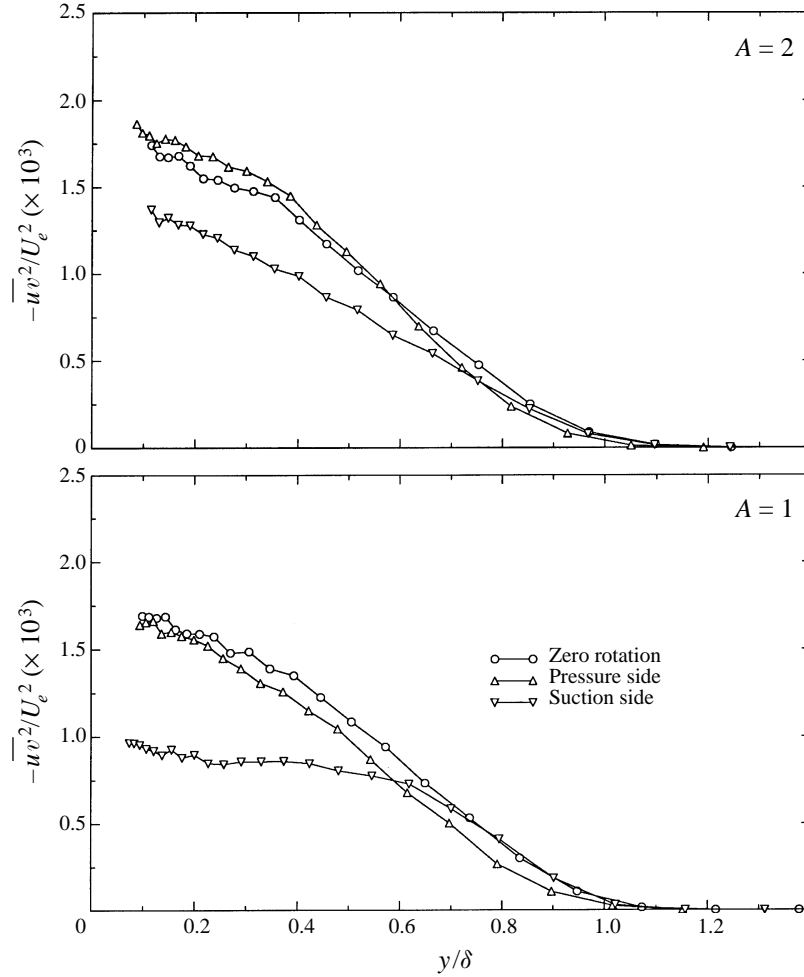


FIGURE 25. As figure 24 but at Station 4.

3.4.2. Pre-multiplied spectra

Selected spectra for the u -component are shown in pre-multiplied form. The profiles were normalized such that the area under each curve is equal to unity. The energy contribution over a given wavenumber range is represented by the area under the curve. So this presentation allows the distribution of energy over the range of wavenumbers to be considered.

Figures 27 and 28 show pre-multiplied u -spectra measured at station 4, at $y/\delta = 0.11$ and $y/\delta = 0.30$ respectively. The u -spectra pressure-side results generally show an increase in the low-wavenumber energy content and a corresponding reduction in the peak. The converse is observed in the suction side. There is no observable shift in wavenumber for the peak of the pre-multiplied profile. The high-wavenumber end of the $A = 2$ profiles are generally unchanged with rotation. Observations from the w -component spectra (not shown here) generally agree with the u -spectra. The variation in low-wavenumber energy is smaller than that observed in the u -spectra.

The $A = 1$ pressure-side case shows a significant bodily shift of the curve to the left or lower wavenumber. For the suction-side $A = 1$ case a shift to the right is observed. The bodily shift remains, but becomes less prominent as the value of y/δ increases. The

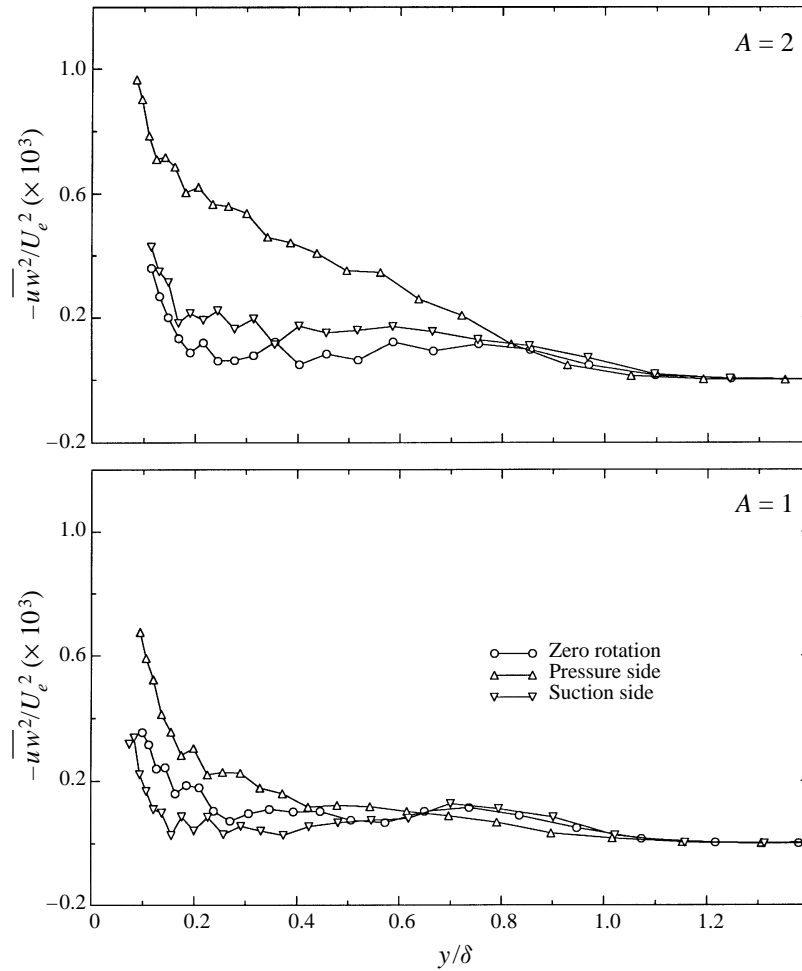


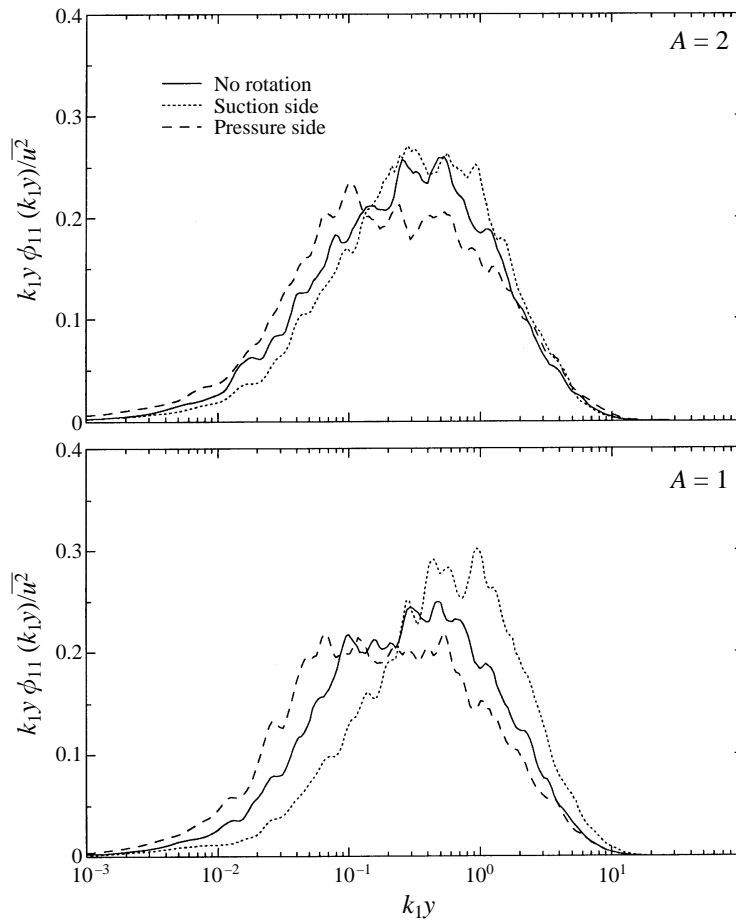
FIGURE 26. Station 4 Reynolds shear stress, $\overline{u'w'}/U_e^2$ vs. y/δ ; aspect ratio as marked.

bodily shift in the $A = 1$ case v -spectrum profiles (not shown here) is consistent with, but somewhat smaller than, the shift observed for the u -spectrum. The bodily shift must be a result of the extra strain rate dW/dz imposed by the secondary flows. On the suction side $dW/dz < 0$ and on the pressure side $dW/dz > 0$.

4. Conclusion

4.1. Cross-stream-plane measurements

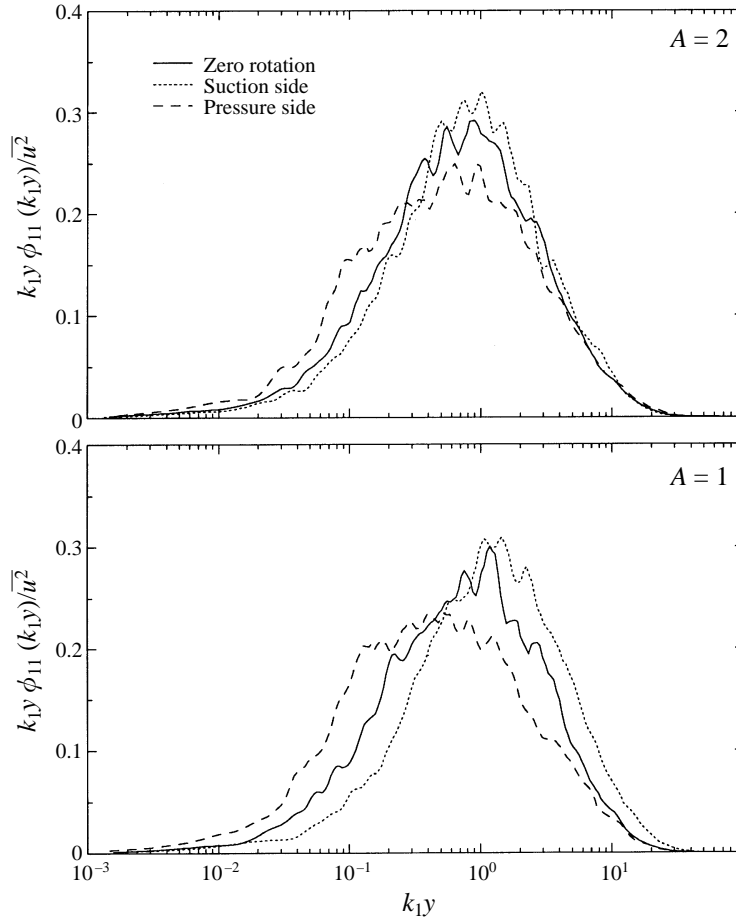
Cross-stream plane vector plots and corresponding integrated streamline patterns clearly identified the secondary flow pattern. The plots demonstrated qualitatively that the secondary flow strength increased with streamwise distance. It was observed that the secondary flow had a negligible impact on the $A = 4$ centreline boundary layer measurements and a weak impact on the $A = 2$ boundary layer at the most downstream station. A strong influence was seen on the $A = 1$ case, particularly at the most downstream station.

FIGURE 27. Pre-multiplied station 4 u -spectra, $y/\delta = 0.11$.

4.2. Secondary flow parameter

The secondary flows introduced an extra strain rate dW/dz in the centreline boundary layer measurements. Following Panchapakesan *et al.* (1996), a divergence parameter was suggested to quantify secondary flow strengths of the form $\beta_D = (\delta^*/U_\tau)S(dw/dz)$. The dW/dz -term was estimated through a ‘first-order’ analysis involving a number of assumptions. The resulting estimation of dW/dz agreed with the cross-stream-plane results at least to first order. Evaluation of dW/dz involved a number of instances of fitting specific experimental data from the current investigation. Consequently, the estimation is not universally applicable; however, it could be applied to zero-pressure-gradient rotating flows to estimate the significance of secondary flow effects. It was suggested that secondary flows strongly influenced the boundary layer development for $\beta_D > 4.6$.

In many practical turbo-machinery problems, geometries and rotational speeds dictate that secondary flows will have a significant effect. In order to model computationally such flow cases, both direct Coriolis effects and extra strain rates induced by secondary flows must be included. The detailed boundary layer measurements presented provide a data base for researchers endeavouring to perform that task.

FIGURE 28. Pre-multiplied station 4 u -spectra, $y/\delta = 0.30$.

4.3. Boundary layer measurements for flow subject to Coriolis force and secondary flow effects

The results showed that the characteristics of the boundary layer strongly perturbed by secondary flows were significantly different to the isolated effects of Coriolis forces. An important feature of the results was the large reduction in skin friction where secondary flows were present. This suggests the stall regime of a rotating diffuser will be influenced by secondary flows. Where strong secondary flows were present the streamline convergence/divergence effects dominated the boundary layer development. Secondary flows did not alter the change in slope of the log law as affected by rotation. The work of Panchapakesan *et al.* (1996), Saddoughi & Joubert (1991) and Hafez (1991) could be utilized in examining and improving prediction techniques for the streamline convergence/divergence case. This could then be coupled with improved modelling of direct Coriolis force effects and an appropriate secondary flow model to accomplish prediction of rotating boundary layers with secondary flows.

5.4. Boundary layer modelling in complex flows

Galperin & Kantha (1989) present a stress equation model for computation of rotating flows. They extend a turbulence model that has been successfully applied to atmospheric boundary layer flows to include rotation and suggest that the model is

suitable for use in prediction of turbo-machinery flows. One of the strengths of this model is that the effects of rotation on the various Reynolds stress components are directly accounted for through transport equations for each component. However, as pointed out by Stubble & Riopelle (1990) in their comment on the work of Galperin & Kantha (1989), rotation 'also directly affects the dissipation rate of turbulent kinetic energy and therefore affects the turbulence time and length scales'. This comment is in agreement with the data presented in Macfarlane (1997) where dissipation is shown to be influenced by rotation. They suggest the need for caution in applying a model that was successful in weak-rotation flow cases to the strong-rotation flow case of turbo-machinery. This highlights the need for experimental data of the type presented to allow testing and tuning of prediction techniques as they become more involved and are used to examine more complex flow cases.

This work was funded through the Australian Research Council and their support is gratefully acknowledged.

REFERENCES

- BRADSHAW, P. 1973 Effects of streamline curvature on turbulent flow. *AGARDograph* 169. NATO.
- ERM, L. P. 1988 Low Reynolds number turbulent boundary layers. PhD thesis, University of Melbourne, Australia.
- ERM, L. P. & JOUBERT, P. N. 1991 Low Reynolds number turbulent boundary layers. *J. Fluid Mech.* **230**, 1–44.
- GALPERIN, B. & KANTHA, L. H. 1989 Turbulence model for rotating flows. *AIAA J.* **27**, 750–757.
- HAFEZ, S. M. 1991 The structure of accelerated turbulent boundary layers. PhD thesis, University of Melbourne, Australia.
- HEAD, M. R. & PATEL, V. C. 1970 Improved entrainment method for calculating boundary layer development. *Aero. Res. Council. R & M* 3643.
- HILL, P. G. & MOON, I. M. 1962 Effects of Coriolis forces on the turbulent boundary layer in rotating machines. *Rep.* 69. Gas Turbine Laboratories, MIT.
- IBAL, G. 1990 Adverse pressure gradient and separating turbulent boundary layer flows with system rotation. PhD thesis, University of Melbourne, Australia.
- IBAL, G. & JOUBERT, P. N. 1995 An experimental study of adverse pressure gradient and separating turbulent boundary layers with system rotation: Part 2 broadband turbulent results. In *The Sixth Asian Congress of Fluid Mechanics, National University of Singapore, Singapore*, pp. 309–312.
- JOHNSON, J. P., HALLEEN, R. M. & LEZIUS, D. K. 1972 Effects of rotation on the structure of two-dimensional fully developed turbulent channel flow. *J. Fluid Mech.* **56**, 533–557.
- KEHL, A. 1943 Untersuchungen über konvergente und divergente, turbulente Reibungsschichten. *Ing Archive.* **13**, 293–329.
- KIKUYAMA, K., MURAKAMI, M., OSHIRO, M., ADACHI, M., HARA, S. & LEE, K. 1986 Effects of Coriolis force on the turbulent boundary layer with pressure gradients. *Bull. JSME* **29**, 2462.
- KLEBANOFF, P. S. 1955 Characteristics of turbulence in a boundary layer with zero pressure gradient. *NACA Tech. Note* 1247.
- KOYOMA, H. S., TAMURA, E. & SAITO, T. 1989 Effect of Coriolis force on developing channel flow. *Proc. 10th Australasian Fluid Mech. Conf., University of Melbourne, Melbourne, Australia.*
- MACFARLANE, I. 1997 Turbulent boundary layers with system rotation. PhD thesis, University of Melbourne, Australia.
- MACFARLANE, I. & JOUBERT, P. N. 1992 Secondary flows in low-Reynolds number adverse pressure gradient rotating boundary layers. *Proc. 11th Australasian Fluid Mech. Conf., University of Tasmania, Hobart, Australia.*
- MACFARLANE, I. & JOUBERT, P. N. 1995 Effects of secondary flows on developing, turbulent, rotating boundary layers. *Proc. 12th Australasian Fluid Mech. Conf., University of Sydney, Sydney, Australia.*

- MACFARLANE, I. & JOUBERT, P. N. 1996 Effects of secondary flows on developing, turbulent, rotating boundary layers – turbulence measurements. *Engineering Turbulence Modelling and Experiments* 3, (ed. W. Rodi & G. Bergeles), p. 571. Elsevier.
- MACFARLANE, I. & JOUBERT, P. N. 1998 Effects of secondary flows on developing, turbulent, rotating boundary layers. *Exp. Thermal Fluid Sci. Special Edition* 17, 79–89.
- MACMILLAN, F. A. 1956 Experiments on pitot tubes in shear flows. *Aero. Res. Council. R. & M.* 3028.
- MOON, I. M. 1964 Effects of Coriolis forces on the turbulent boundary layer in rotating fluid machines. *Rep. 89 Gas Turbine Laboratories, MIT.*
- MOORE, J. 1967 Effects of Coriolis on turbulent flow in rotating channels. *Rep. 69 Gas Turbine Laboratories, MIT.*
- NICKELS, T. B. & JOUBERT, P. N. 1997 Equilibrium turbulent boundary layers with extra rates-of-strain. *J. Fluid Mech.* (submitted).
- PANCHAPAKESAN, N. R., NICKELS, T. B., JOUBERT, P. N. & SMITS, A. J. 1997 Lateral straining of turbulent boundary layers. Part 2. Streamline convergence. *J. Fluid Mech.* 349, 1–30.
- PATEL, V. C. 1965 Calibration of the Preston tube and limitations on its use in pressure gradients. *J. Fluid Mech.* 23, 185.
- PERRY, A. E. 1982 *Hot-Wire Anemometry*. Oxford University Press.
- PERRY, A. E., HENBEST, S. & CHONG, M. S. 1986 A theoretical and experimental study of wall turbulence. *J. Fluid Mech.* 165, 163.
- SADDOUGHI, S. G. & JOUBERT, P. N. 1991 Lateral straining of turbulent boundary layers. Part 1. Streamline divergence. *J. Fluid Mech.* 229, 173–204.
- STUBLEY, G. D. & RIOPELLE, G. 1990 Comment on ‘Turbulence Model for Rotating Flows’. *AIAA J.* 28, 1530.
- TOWNSEND, A. A. 1976 *The Structure of Turbulent Shear Flow*. Cambridge University Press.
- WATMUFF, J. H., WITT, H. T. & JOUBERT, P. N. 1985 Developing turbulent boundary layers with system rotation. *J. Fluid Mech.* 157, 405–448.
- WITT, H. 1986 Effects of rotation on turbulent boundary layers and wakes. PhD thesis, University of Melbourne, Australia.